Petroleum Science 23 (2026) 5723–5737

Contents lists available at ScienceDirect

Petroleum Science

journal homepage: www.keaipublishing.com/en/journals/petroleum-science

Original Paper

Dynamic evolution of non-uniform water invasion in deformed multi-scale porous media retrieved by computed tomography

Fang-Zhou Liu [a], Dai-Gang Wang [a,b,*], Yu-Shan Ma [a], Ning-Hong Jia [c], Jun-Lei Wang [c,**], Chao-Zhong Qin [d], Fa Zhang [c], Kao-Ping Song [a], Yu-Hua Liu [a], Cheng-Ming Li [a]

[a] State Key Laboratory of Petroleum Resources and Engineering, China University of Petroleum (Beijing), Beijing, 102249, China
[b] State Key Laboratory of Deep Oil and Gas, China University of Petroleum (East China), Qingdao, 266580, Shandong, China
[c] Research Institute of Petroleum Exploration and Development, PetroChina, Beijing, 100083, China
[d] State Key Laboratory of Coal Mine Disaster Dynamics and Control, Chongqing University, Chongqing, 400044, China

A R T I C L E I N F O

Article history:
Received 30 November 2025
Received in revised form
9 February 2026
Accepted 15 April 2026
Available online 22 April 2026

Edited by Meng-Jiao Zhou

Keywords:
Ultra-deep reservoir
Dynamic characteristics of water invasion
Multiphase flow
Pore scale
CT scan

A B S T R A C T

Ultra-deep sandstone gas reservoirs have great potential for exploration and development and have become a major focus worldwide. Under the influence of ultra-high temperature, pressure and strong in-situ stress, the mechanical properties of rocks change significantly, resulting in the coexistence of diverse pores and fractures. This rock deformation, coupled with severely non-uniform water invasion, fundamentally hinders efficient reservoir development by promoting preferential flow channeling and early water breakthrough, which reduce sweep efficiency and increase remaining gas retention. In this paper, a microfocus CT scanning experiment is conducted on ultra-deep rock under in-situ stress loading. Based on the acquired scans, three-dimensional digital cores representing the deformed multi-scale fracture-pore media are reconstructed under various stress conditions. Dynamic pore network simulations are performed to systematically investigate gas-water migration and distribution characteristics under the effects of stress, displacement pressure difference and fracture conductivity. The research shows that stress is the most critical factor governing the water invasion process. In the absence of applied stress, water preferentially invades well-connected pores, exhibiting a regular front and fast migration rate, while gas remains in small, poorly connected blind pores. When the stress is loaded to the linear elastic deformation stage, the core exhibits increased radial deformation, and pronounced dynamic changes occur during the water invasion process. Remaining gas easily accumulates in isolated pores at corner or dead-end regions, and a large amount of remaining gas appears in regions with low driving force. Upon reaching the plastic deformation stage, localized fracturing occurs, which increases the number of throats and enhances connectivity. This leads to a transition of the water invasion mode from uniform to non-uniform. In the fracture stage, the water phase preferentially moves along the fracture surface rapidly, thereby accelerating the water invasion process. The local pressure distribution between the fracture and the matrix is uneven, inducing the wetting phase fluid to continuously seep from the fracture into the matrix, expanding the swept range. Fracture conductivity directly affects the migration speed and morphology of the water invasion front, but its impact on the final water invasion effect is weak.

1. Introduction

Natural gas is increasingly recognized as the most realistically sustainable, stably supplied, and environmentally cleanest low-carbon fossil fuel source in the energy industry (Jia et al., 2024). In recent years, global oil and gas exploration efforts have rapidly expanded from conventional medium and shallow reservoirs to deep and ultra-deep targets. Due to the great burial depth, high

* Corresponding author.
** Corresponding author.
E-mail addresses: dgwang@cup.edu.cn (D.-G. Wang), wangjunlei@petrochina.com.cn (J.-L. Wang).

Peer review under the responsibility of China University of Petroleum (Beijing).

https://doi.org/10.1016/j.petsci.2026.04.028

formation pressure and temperature, and complex petrophysical properties, ultra-deep sandstone reservoirs exhibit an exceptionally complex pore structure and flow mechanism, characterized by the coexistence of various pore types and natural fractures (Li et al., 2014; Zhang et al., 2022; Shi et al., 2024). The presence of fractures and high-permeability streaks makes these gas reservoirs highly susceptible to rapid, non-uniform water invasion, which further exacerbates reservoir heterogeneity and flow complexity, consequently impairing reservoir performance (Liu et al., 2022, 2023; Hu et al., 2024). Moreover, the mechanical behavior of deep rocks deviates significantly from their shallow counterparts, particularly concerning their deformation and failure processes. Accurately characterizing the complex structure of ultra-deep sandstone reservoirs and precisely predicting the fluid flow behavior under stress-induced deformation remain key technical challenges for the efficient development of these valuable resources (Chen et al., 2024).

Extensive studies have been conducted on multiphase flow and remaining gas occurrence characteristics in ultra-deep sandstone reservoirs using various methodologies, including core flooding experiments (Wang et al., 2020; Tang et al., 2025), nuclear magnetic resonance (NMR) (Birdwell and Washburn, 2015; Xin et al., 2022; Xiao et al., 2019) and microfluidic visualization experiments (Fang et al., 2019; Hu et al., 2025). Al-Zaidi et al. (2019) investigated the influence of fluid pressure and temperature on the water intrusion patterns in sandstone cores. Guo et al. (2020) used NMR technology to analyze the distribution of gas and water during water flooding. Han et al. (2023) utilized core displacement and NMR experiments to evaluate the distribution of crude oil in core pores during water invasion. Their research results showed that water invasion mainly occurred in mesopores and macropores. Hu et al. (2024) studied the influence of carbonate pore structure characteristics on gas-water percolation characteristics by combining cast thin sections, Scanning Electron Microscopy (SEM), and NMR experiments, and their findings suggested that the presence of vugs enhanced the gas storage capacity and improved gas-water percolation capabilities near the vugs. However, both core displacement experiments and NMR experiments cannot directly observe the dynamic migration and distribution characteristics of gas–water two-phase flow, lacking intuitive visualization. In recent years, microfluidic chip technology has begun to be applied to experimentally characterize the flow mechanisms of oil and gas reservoir percolation at the nano-micro scale. Microfluidic chips possess good light transmission performance, allowing direct observation of the gas–water distribution during the displacement process. Lu et al. (2019) utilized 3D printing technology to fabricate microfluidic chips for gas–water two-phase displacement experiments, observing the gas-water distribution during both the water invasion (water-drive gas) and the gas accumulation (gas-drive water). However, simulating ultra-deep conditions poses significant challenges. The behavior of rock and fluids under high-temperature and high-pressure reservoir conditions differs substantially from that under conventional conditions. Furthermore, the thin physical models employed in microfluidic experiments cannot withstand high pressure and therefore fail to accurately represent the true gas-water distribution or the non-uniform water invasion laws characteristic of ultra-deep sandstone gas reservoirs.

Over the past decade, pore-scale simulation has increasingly become a powerful tool for investigating complex pore-scale flow mechanisms (Blunt et al., 2013). Zhang et al. (2021) used the Shan Chen lattice Boltzmann method (SC-LBM) to simulate pore-scale gas-water two-phase flow. Shi et al. (2023) generated non-uniform porous media using the Quartet Structure Generation Set (QSGS) method, simulating displacement processes with the phase field method and comparing the influence of different capillary numbers. Yang et al. (2022) established physical models of deep cores through CT scanning, simulated gas-water two-phase flow using the volume of fluid method, analyzing the effects of wettability and capillary number on fluid distribution. Zhang et al. (2023) developed a multiple-relaxation-time color-gradient lattice Boltzmann model for simulating gas–water two-phase flow. Their study shows that, during water invasion in carbonate gas reservoirs, blind-end pore-trapped gas and pore-throat constriction-trapped gas are determined by the structure of individual pores, while bypass-trapped gas, “H-type” trapped gas, and network-type trapped gas are governed by the matching relationships among pores. Zhang et al. (2015) simulated gas-water two-phase flow in digital rock using the color-gradient lattice Boltzmann method, and the results indicate that the higher the gas–water density ratio, the more obvious the viscous fingering phenomenon. Despite these advances, existing simulation methods face significant challenges when applied to ultra-deep sandstone. Specifically, experimental characterization of the complex pore structure of ultra-deep sandstone remains difficult. Under the influence of strong stress, the dynamic deformation of the pore structure and fractures in the rock intensifies the microscopic heterogeneity of the reservoir, resulting in an extremely complex gas-water flow law of multi-scale fracture-pore media.

In this study, a typical ultra-deep sandstone in the Tarim Basin is selected as the research object. A high-resolution micro-focus CT system is utilized to perform imaging scans during the in-situ stress loading process. Using image reconstruction techniques, digital models of ultra-deep the sandstone are established at different stress loading stages. On this basis, dynamic pore-network simulations of gas–water two-phase flow in the deformed multi-scale media are conducted. The primary objective is to investigate the dynamic migration and distribution characteristics of the fluids under the influences of stress, displacement pressure difference and fracture conductivity, thereby analyzing the non-uniform water invasion behavior specific to ultra-deep sandstone gas reservoir deformation.

2. In-situ micro X-ray CT scanning experiment of ultra-deep sandstone

Using ultra-deep sandstone core as the research object, in-situ stress loading micro-focus CT scanning experiments are employed to conduct staged scanning of the uniaxial compression process. Through image reconstruction, the internal structural space and failure morphology of the ultra-deep sandstone are visualized, and four pore network models corresponding to different stress levels are constructed for subsequent pore network modeling.

2.1. Experimental samples and methods

A sandstone core is taken from an ultra-deep gas reservoir in the Tarim Basin, with a density of 2.217 g/cm^3, a porosity of 16.771%, and a permeability of 52.747 mD. According to the recommended standards of the International Society of Rock Mechanics, the core is processed into standard cylindrical specimens with a diameter of 4 mm and a height of 8 mm. Two cylindrical sandstone specimens are prepared for this study. Specimen A is used for a conventional uniaxial compression test without CT scanning as a pre-test, while Specimen B is used for an in-situ uniaxial compression test combined with CT imaging.

The experimental system mainly consists of a stress loading device and an X-ray CT scanning system. The loading system used in this study is a micro-mechanical testing device manufactured by DEBEN (UK), which adopts a compact rigid-frame structure and provides stable and controllable displacement-controlled loading. The device has a maximum load capacity of 5 kN. For the cylindrical sandstone specimens with a diameter of 4 mm used in this study, this corresponds to a maximum achievable axial stress of approximately 398 MPa. Uniaxial compression is applied under displacement control at a constant loading rate of 0.03 mm/min. X-ray CT scanning is performed using a three-dimensional X-ray microscope (Xradia Versa 520) (Duan et al., 2018), which mainly consists of an X-ray source (90 kV in voltage and 89 μA in current), a rotating stage and a detector. The system employs a combination of geometric and optical magnification, enabling high image contrast and spatial resolution. By mounting the loading device on the rotating stage of the CT system, in-situ loading and synchronous CT imaging of the sandstone specimens are achieved.

A conventional uniaxial compression test without CT scanning is first conducted on Specimen An under the same loading conditions to obtain the reference stress–strain curve and characteristic strain levels. Based on the pre-test results of Specimen A, an in-situ uniaxial compression test combined with real-time CT scanning is then performed on Specimen B to investigate pore structure evolution during the compression–failure process. Four CT scans are conducted at strain levels corresponding to 0%, 50%, and 90% of the reference peak strain, as well as at failure. To account for the inherent heterogeneity of sandstone, the strain levels are defined relative to the reference peak strain rather than absolute strain values. Each CT scan acquired 1000 projection images with a voxel resolution of 5 μm. Prior to loading, an initial stress is applied to ensure complete contact between the core end face and the bearing plate. The stress is then applied at a constant rate of 0.03 mm/min. The loading is stopped upon reaching the predetermined condition for the first scan. After the CT scan is completed, loading resumes to the next level, and the cycle is repeated until the final (fourth) scan is completed.

The CT images are processed and reconstructed using the open-source software ImageJ (Collins, 2007). Prior to digital core reconstruction, the grayscale CT images are denoised using a median filtering method to suppress high-frequency noise while preserving pore boundaries. To avoid boundary effects and ensure representativeness, a three-dimensional representative elementary volume (REV) is extracted from the central region of the core, with a size of 600 × 300 × 300 voxels, corresponding to a physical size of 3000 × 1500 × 1500 μm^3. The filtered images are segmented into binary images to distinguish pore space from the solid matrix using a global threshold segmentation method based on grayscale intensity differences (Liu et al., 2025). The threshold value is determined through a combination of grayscale histogram analysis and visual inspection to ensure accurate identification of pore structures. The segmented binary images are stacked sequentially to construct three-dimensional digital core models that preserve the spatial distribution and connectivity of pore structures. Based on the reconstructed digital cores, equivalent pore network models are extracted using the porous media image analysis toolset PoreSpy (Gostick et al., 2019). A watershed-based algorithm is employed to partition the pore space into individual pores and throats. Subsequently, topological and geometric properties of the pore network, including coordination number and shape factor, are calculated. The extracted pore network models are visualized using ParaView software (Ayachit et al., 2015).

2.2. Experimental results and analysis

The stress-strain curve of sandstone core under uniaxial compression is shown in Fig. 1, and the red dots in the figure represent different CT scanning stages. It can be seen from the figure that the stress-strain curve of ultra-deep sandstone core can be divided into 4 stages: linear elastic deformation stage, plastic deformation stage, post-peak plastic deformation stage and residual strength stage. The peak strength of the core is 44.97 MPa and the peak strain is 1.39%.

The 3D digital core REVs obtained by CT scanning under different stress levels are shown in Fig. 2(a), with corresponding binary models presented in Fig. 2(b). The results show that the core exhibits good microscopic connectivity in the initial state. As the stress increases, the large pores in the middle of the core shrink. When the stress reaches 44.97 MPa, some pores close completely, leading to a deterioration of pore connectivity. Upon core failure, a distinct, single shear fracture penetrates the entire rock sample. The results of the equivalent pore network under different stress levels are shown in Fig. 2(c). Statistical analysis shows the average pore radius follows a trend of initial decrease, followed by a significant increase post-failure, measuring 7.0848 × 10^{-6} m (0 MPa), 7.0493 × 10^{-6} m (30.86 MPa), 6.9375 × 10^{-6} m (44.97 MPa) and 7.6987 × 10^{-6} m (break), respectively.

The porosity and permeability of ultra-deep sandstone cores under different loading levels are shown in Table 1. In the initial state, the porosity of the core is 14.434%, and the permeability of single-phase flow simulation is 49.472 mD. The simulation results show good agreement with the experimental data. During the initial stage of stress loading, some pores are compressed and transformed into smaller pores, resulting in a slight decrease in porosity and permeability. When the stress increases to 44.97 MPa, some pores close, but the onset of micro-fracturing leads to an increase in the number of throats and enhanced local connectivity. This structural change results in a significant increase in porosity and a recovery increase in core permeability. After core failure, both the porosity and permeability increase significantly due to the formation of macro-fractures.

The frequency histograms of pore and throat radius distributions of the ultra-deep sandstone under different stress levels are shown in Fig. 3. The pore radius distribution is relatively concentrated and approximately a normal distribution. When the stress increases to 44.97 MPa, the peak of the pore radius frequency distribution curve rises and shifts to the left, indicating the appearance of a large number of small pores at this time. After core

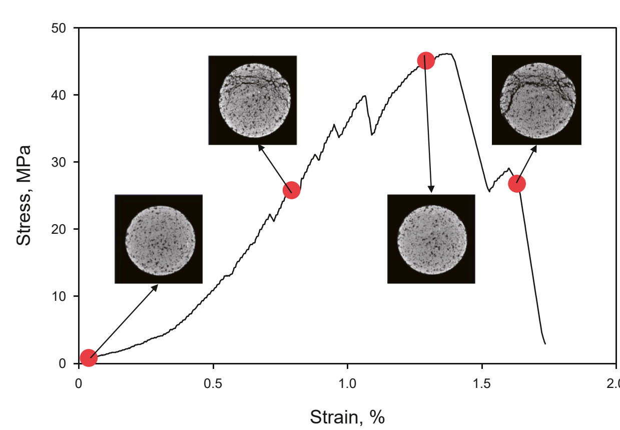

Fig. 1. Stress-strain curve of ultra-deep sandstone core.

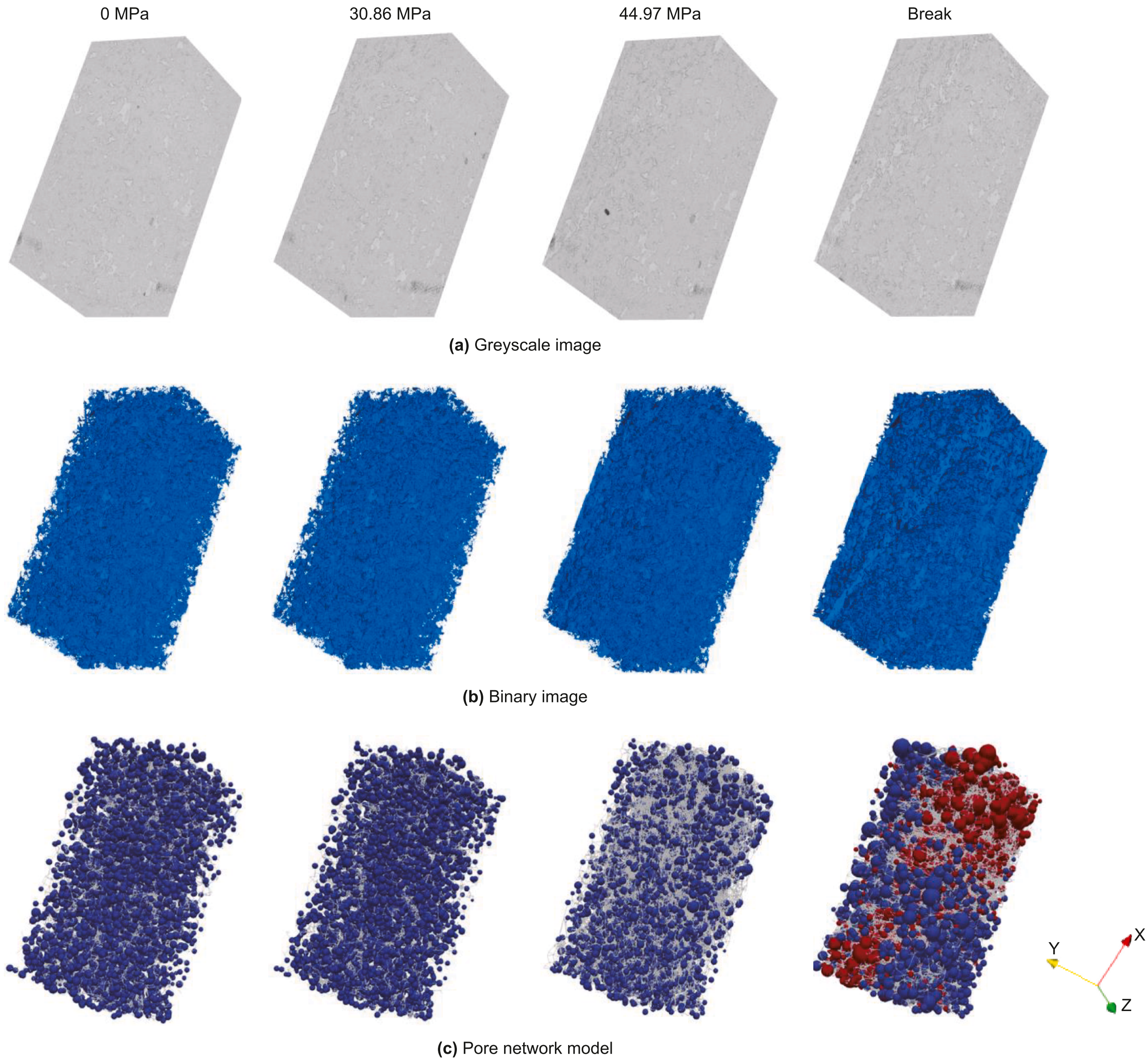

Fig. 2. Digital models of ultra-deep sandstone core.

Table 1
Physical properties of cores under different stress conditions.

	0 MPa	30.86 MPa	44.97 MPa	Break
Porosity, %	14.43	13.39	20.97	37.42
Permeability, mD	49.47	35.34	47.12	61.45

failure, a large number of new macropores are generated in the failure zone. The peak of the pore radius distribution frequency histogram curve shifts to the right, the number of throats increases significantly, and the distribution of throat radius distribution tends to be concentrated.

To quantitatively characterize the heterogeneity of pore–throat size distributions, the heterogeneity index H is introduced. The index H is defined as the coefficient of variation of the pore (or throat) radius distribution: $H = \sigma_r / \bar{r}$, where $\bar{r}$ is the mean pore (or throat) radius and σ_r is the corresponding standard deviation. A larger H value indicates a higher degree of dispersion in pore size distribution and thus stronger structural heterogeneity.

The frequency histograms of pore body and pore throat radius distributions under different stress levels are shown in Fig. 3. Under low stress conditions (0 and 30.86 MPa), both pore body radius and pore throat radius are mainly distributed in a narrow range from 2×10^{-5} m to 6×10^{-5} m, with well-defined peaks, indicating a relatively homogeneous pore–throat structure. Correspondingly, the heterogeneity index H remains stable, with values of 0.63–0.64 for pore bodies and 1.26 for pore throats, reflecting a low degree of pore size dispersion.

When the stress increases to 44.97 MPa, the peak of the pore body radius distribution shifts toward smaller radius, while the overall distribution range expands to 2×10^{-5} – 10×10^{-5} m, indicating the coexistence of newly generated small pores and pre-existing larger pores. The pore throat radius distribution exhibits a similar broadening trend. At this stage, the heterogeneity index H increases markedly to 1.94 for pore bodies and 2.38 for pore throats, demonstrating a significant enhancement in pore–throat size variability.

After core failure, pore–throat heterogeneity is further intensified. The pore body radius distribution expands to a wide range

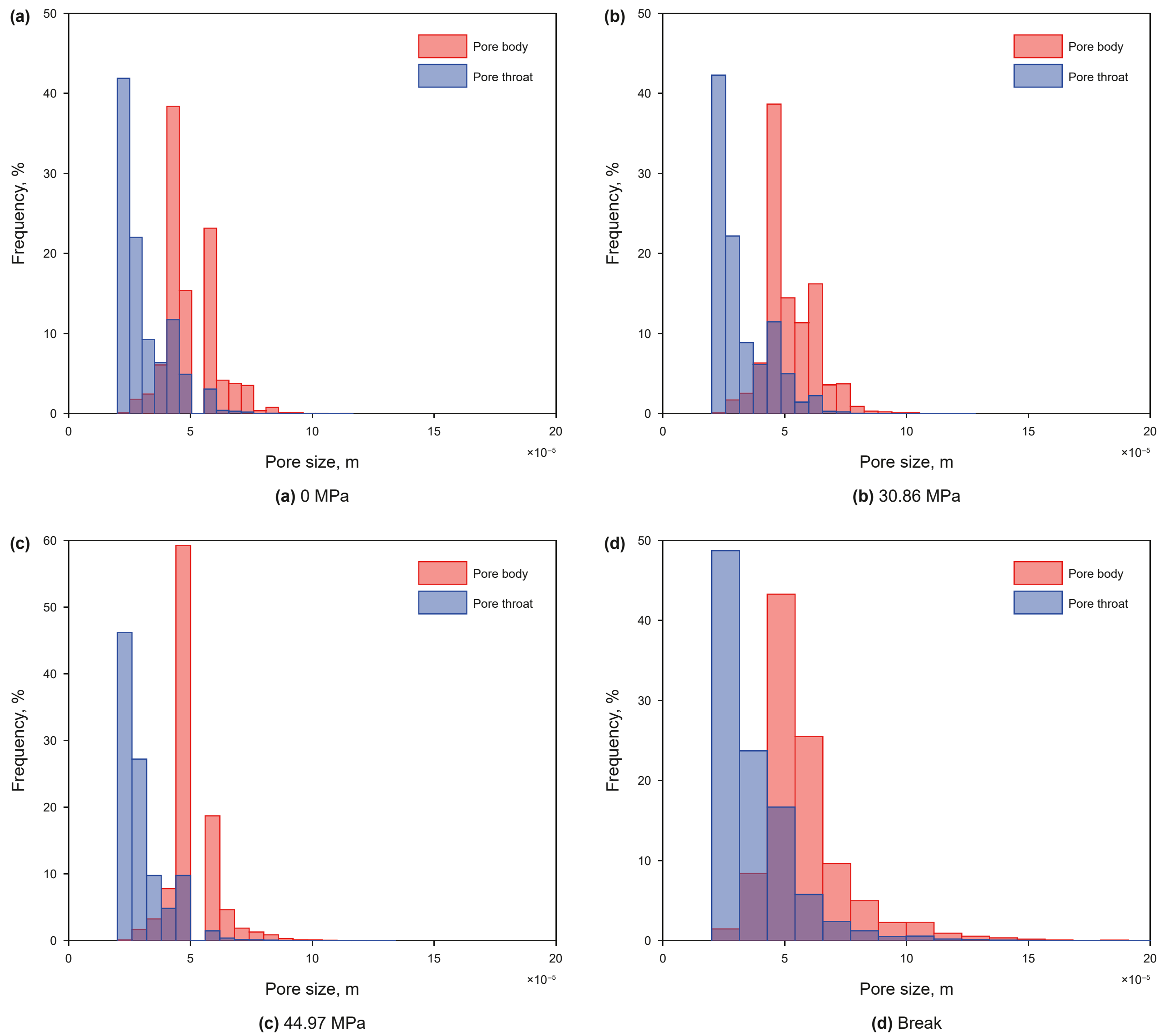

Fig. 3. Frequency histogram of pore/throat radius distribution.

of 2×10^{-5} m to 18×10^{-5} m and develops a pronounced right-skewed long tail, while the pore throat radius distribution also shows a substantially increased spread. Correspondingly, H increases to 2.3 for pore bodies, while it increases to 2.66 for pore throats. These quantitative results consistently demonstrate that stress-induced damage and failure lead to a pronounced enhancement of pore–throat structural heterogeneity.

The coordination number refers to the number of independent throats connected to a pore, which characterizes the connectivity of pore networks and serves as an important parameter for evaluating the transport properties of porous media (Xu et al., 2018). A statistical analysis of the coordination numbers of sandstone cores under different stress levels is shown in Fig. 4(a). Under low stress conditions (0 and 30.86 MPa), the coordination number distribution is relatively concentrated, with most pores exhibiting coordination numbers lower than 10 and a well-defined dominant peak. As stress increases to 44.97 MPa, the peak of the distribution shifts toward lower coordination numbers, indicating the progressive closure of pore–throat connections and a reduction in local connectivity prior to failure. After core failure, the coordination number distribution changes markedly. Pores with high coordination numbers appear, and the upper tail of the coordination number distribution extends beyond 30, reflecting the formation of fracture-induced connections. This results in a highly non-uniform enhancement of pore network connectivity, where a limited number of highly connected pores dominate fluid transport. Such redistribution of coordination numbers quantitatively demonstrates the enhancement of pore network heterogeneity and the significant increase in overall flow capacity induced by fracturing.

The shape factor is employed to characterize the geometric regularity of pore–throat cross sections in the pore network. It is defined as $G = 4\pi A/P^2$, where A is the cross-sectional area of a pore or throat, P is the corresponding perimeter (An et al., 2016). This parameter is calculated based on the pore network models extracted from the CT-reconstructed digital cores using the

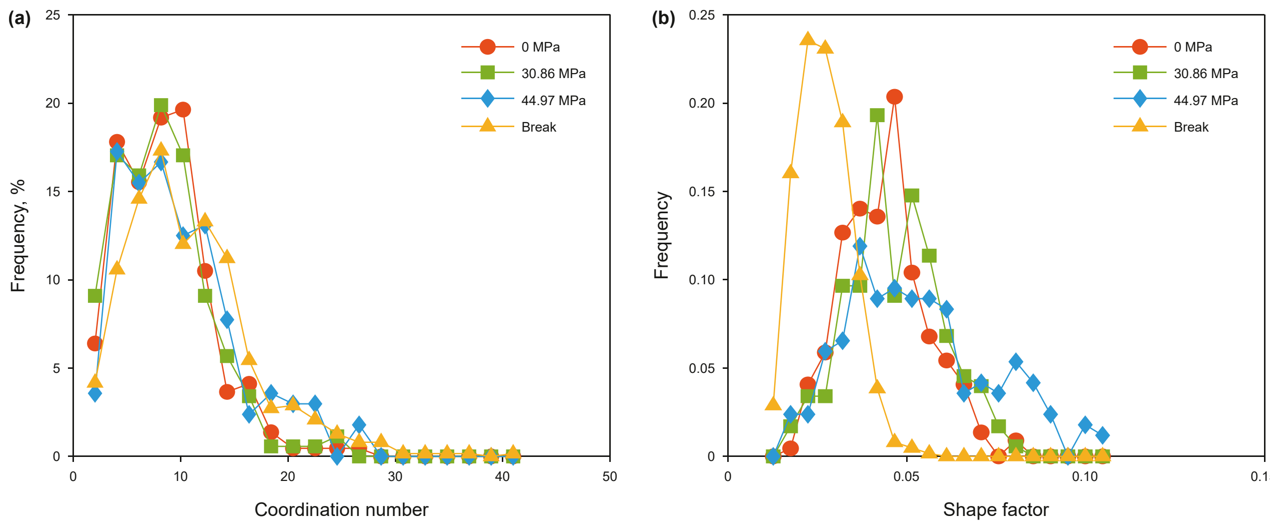

Fig. 4. Frequency distribution curves of coordination number and shape factor under different stress conditions. **(a)** Coordination number, **(b)** shape factor.

PoreSpy toolset. A larger shape factor indicates a more regular and circular pore–throat geometry, whereas smaller values correspond to more irregular and complex shapes.

The frequency curves of shape factor distributions under different stress levels are shown in Fig. 4(b). Under low stress conditions (0 and 30.86 MPa), the shape factor distribution exhibits a clear peak in the range of 0.045–0.055, with most values distributed between 0.03 and 0.07, indicating that the majority of pore–throat cross sections maintain relatively regular geometries. As stress increases to 44.97 MPa the peak of the shape factor distribution shifts toward lower values, mainly concentrated in the range of 0.035–0.045. Meanwhile, the proportion of pore–throat cross sections with shape factor values lower than 0.03 increases noticeably, reflecting a progressive increase in pore–throat geometric irregularity induced by stress. After core failure, the shape factor distribution becomes strongly dominated by low values, with the main peak concentrated in the range of 0.02–0.03 and most values remaining below 0.04. This systematic redistribution of shape factor values indicates that fracture development and stress-induced damage significantly increase pore–throat geometric heterogeneity.

3. Dynamic pore network simulation method for two-phase flow

Dynamic pore network simulation is a powerful method used to investigate the transient flow phenomena of multiphase flow at the pore scale, explicitly incorporating the coupled effects of capillary pressure and viscous forces.

In the simulation of gas-water two-phase dynamic pore networks, the following fundamental assumptions are typically adopted: (1) The entire pore space is idealized as a network composed of pores and throats. Flow between pores is governed by the mass conservation law, with energy dissipation occurring exclusively within the throats (David et al., 1993); (2) Capillaries with circular, square, and triangular cross-sectional shapes are used as the basic pore units (Qin and Van Brummelen, 2019); (3) Two immiscible and incompressible fluid flow within the pore space; (4) Both fluids occupy the pores and throats, but the pressure drop occurs only within the throats; (5) A single, sharp interface exists between the two fluid phases, and diffusion is considered negligible; (6) Fluid movement through the throats is assumed to occur in a piston-like displacement manner; (7) The fluid flow rate is calculated using the Hagen-Poiseuille equation.

3.1. Governing equations

(1) Two-phase flow governing equation.

The local capillary pressure of pore i is defined as:

$$p_i^c = p_i^n - p_i^w = f(s_i^w) \tag{1}$$

The volume conservation equation for fluid a in pore i is as follows (Thompson, 2002):

$$V_i \frac{ds_i^\alpha}{dt} = -\sum_{j=1}^{N_i} Q_{ij}^\alpha, \alpha = n, w \tag{2}$$

where, i is the pore number, ij is the throat number, a is the phase number, n is the non-wetting phase, w is the wetting phase, N_i is the coordination number of the pore i, V_i is the volume, m^3, s_i is the saturation, and Q_{ij} is the flow rate from pore i to pore j, m^3/s.

The volume flux through throat ij is calculated based on the Hagen–Poiseuille equation (Aker et al., 2000):

$$Q_{ij}^\alpha = K_{ij}^\alpha \left(p_i^\alpha - p_j^\alpha\right), \alpha = n, w \tag{3}$$

where K_{ij}^a is the conductivity, $m^3/(Pa \cdot s)$; and p is the pressure, Pa.

The summation of the volume conservation equations for the gas and water phases:

$$\sum_{j \in N_i} Q_{ij}^{tot} = \sum_{j \in N_i} \left(Q_{ij}^n + Q_{ij}^w\right) = 0 \tag{4}$$

By combining Eqs. (1)–(3), the variables s_i^w, p_i^w and p_i^n can be solved.

(2) Pressure field solver.

In order to reduce the computational requirements, the total pressure $\bar{p}_i$ is defined as:

$$\overline{p}_i = s_i^{\rm w} p_i^{\rm w} + s_i^{\rm n} p_i^{\rm n} \tag{5}$$

Among them, the relationship between the wetting phase saturation and the non-wetting phase saturation is:

$$s_i^{\rm w} + s_i^{\rm n} = 1 \tag{6}$$

By combining Eqs. (1), (5) and (6), the pressure calculation equations for the wetting-phase and non-wetting-phase fluids are obtained:

$$p_i^{\rm w} = \overline{p}_i - s_i^{\rm n} p_i^{\rm c} \tag{7}$$

$$p_i^{\rm n} = \overline{p}_i + s_i^{\rm w} p_i^{\rm c} \tag{8}$$

By combining the above equations, the mixed pressure equation is obtained (Aker et al., 2000; Joekar-Niasar et al., 2010):

$$\sum_{j=1}^{N_i} \left(K_{ij}^{\rm n} + K_{ij}^{\rm w}\right)\left(\overline{p}_i - \overline{p}_j\right) = -\sum_{j=1}^{N_j} \left\{ \left[K_{ij}^{\rm n}(1-s_i^{\rm n}) - K_{ij}^{\rm w} s_i^{\rm n}\right] p_i^{\rm c} + \left[K_{ij}^{\rm w} s_j^{\rm n} - K_{ij}^{\rm n}\left(1 - s_j^{\rm n}\right)\right] p_j^{\rm c} \right\} \tag{9}$$

The coefficients on the left and right sides of the equation are controlled only by saturation, and the diagonal-scaled biconjugate gradient method is employed for numerical solution, with the total pressure as the target variable. The computational implementation relies on the SLATEC Common Mathematical Library, an open-source numerical toolkit developed in Fortran language, which provides a high-precision linear algebra solver and a core algorithm for scientific computing.

(3) Saturation field solver.

After the total pressure is calculated, the two-phase fluid pressure is calculated by Eqs. (7) and (8), and then the flow rate is calculated according to Eq. (3), and the saturation is explicitly updated by Eq. (2).

3.2. Local rules

(1) Fluid competitive filling dynamics.

In the process of water invasion, the topological morphology changes of the liquid-liquid interface are very complex, and the morphology of the pore-filled interface can be classified into two categories: Arc menisci (AM) and Main terminal meniscus (MTM) (Mason and Morrow, 1991). Depending on the flow conditions, the morphology of the pore filling interface can be automatically switched between AM and MTM. Among them, there is a significant difference in the behavior of MTM during displacement and imbibition. During displacement, MTM is formed at the entrance of the throat filled with non-wetting fluid pores, while during imbibition, MTM can span the connected pores and throats. In this paper, MTM filling is initiated in a pore if any of the following three conditions are satisfied: (1) The wetting-phase saturation in the pore exceeds 0.5, at least one connected pore is undergoing MTM filling, and the capillary pressure exceeds the MTM pressure; (2) At least one connected pore experiences snap-off, and the capillary pressure exceeds the MTM pressure; (3) Corner flow cannot occur within the pore.

(2) Fluid conductivity.

If only the non-wetting phase or the wetting phase is present in the pores, the conductivity is (Qin et al., 2021):

$$g = \begin{cases} 0.6GS^2 & \text{triangle} \\ 0.5632GS^2 & \text{square} \\ 0.5GS^2 & \text{circle} \end{cases} \tag{10}$$

where G is the shape factor and S is the pore cross-sectional area. If both the wetting phase and the non-wetting phase are present in the pores, the conductivity of the wetting phase fluid is defined as:

$$\tilde{g}^{\rm w} = \exp\left\{ \left[-18.20\left(\tilde{G}^{\rm w}\right)^2 + 5.88\tilde{G}^{\rm w} - 0.35 + 0.02\sin\left(\beta - \frac{\pi}{6}\right) \right] \Big/ \left(\frac{1}{4\pi} - \tilde{G}^{\rm w} \right) + 2\ln S^{\rm w} \right\} \tag{11}$$

$\tilde{G}^{\rm w}$ is the shape factor of the wetting region, defined as:

$$\tilde{G}^{\rm w} = \frac{\tilde{A}^{\rm w}}{4[1 - (\theta + \beta - \pi/2)\sin\beta/\cos(\theta+\beta)]} \tag{12}$$

$\tilde{A}^{\rm w}$ is the dimensionless wetting area, defined as:

$$\tilde{A}^{\rm w} = \left(\frac{\sin\beta}{\cos(\theta+\beta)} \right)^2 \left(\frac{\cos\theta\cos(\theta+\beta)}{\sin\beta} + \theta + \beta - \frac{\pi}{2} \right) \tag{13}$$

The conductivity of a non-wetting phase fluid is defined as:

$$g^{\rm n} = \begin{cases} 0.6GS^2\left(1 - A^{\rm w}\right)^2 & \text{triangle} \\ 0.5632GS^2\left(1 - A^{\rm w}\right)^2 & \text{square} \end{cases} \tag{14}$$

The formula for calculating the fluid conductivity from pore i to pore j is:

$$K_{ij} = 1 \Big/ \left(\frac{l_i}{2g_i} + \frac{l_j}{2g_j} + \frac{l_{ij}}{g_{ij}} \right) \tag{15}$$

where l is the length, m; g is the conductivity, $m^4/(Pa \cdot s)$.

The numerical calculation procedures and model validation follow the studies by Qin et al. (2021, 2022), in which the dynamic pore network model is systematically validated by comparing numerical simulations with experimental measurements of countercurrent imbibition in cylindrical sandstone cores. In the present study, the same modeling framework, governing equations, and local flow rules are adopted to simulate the gas–water flow processes in porous media. In this work, the model is initially fully saturated with the non-wetting phase (gas). During the simulation, the wetting-phase fluid is injected from the bottom of the core at a constant pressure of 4000.0 Pa, while the pressure at the outlet boundary is maintained constant at 0.0 Pa, and the model is surrounded by a closed boundary. The densities of the gas and water phases are 1.2 kg/m^3 and 1000 kg/m^3, respectively, and their viscosities are 1.79×10^{-5} Pa s and 1.0×10^{-3} Pa s, respectively. The interfacial tension is 0.073 N/m.

4. Results and discussion

To elucidate the non-uniform water invasion patterns within the deformed fracture-pore media of ultra-deep sandstone cores, two-phase gas-water flow simulations are executed utilizing the aforementioned dynamic pore-network model. The migration and distribution characteristics are compared and analyzed under different stress levels, displacement pressure differences and fracture conductivity conditions.

4.1. Effect of stress

The dynamic network simulation of gas-water two-phase flow is carried out under different stress conditions. Fig. 5 illustrates the evolution of the microscopic gas-water distribution under different stress levels (blue represents the water phase, and red represents the gas phase). The results show that when no stress is applied, the water phase mainly invades the pores with good connectivity, and the remaining gas mainly distributes in the small pores with poor connectivity. The water invasion front edge is more regular and the migration rate is faster, but the migration distance is limited. Furthermore, gas entrapped in blind-end pores at the core margins remains largely immobile, as the pressure field induced by the advancing water phase does not effectively extend into these isolated regions. When the stress increases to 30.86 MPa, the wetting phase water preferentially advances along the pore walls and through narrower pore throats, subsequently reaching various small channels. This progression often leads to the isolation of large pores by the surrounding water, thereby generating trapped gas clusters. This process reduces the overall connectivity of the gas phase and diminishes its flow capacity. Moreover, in the central region of the core, where the pore

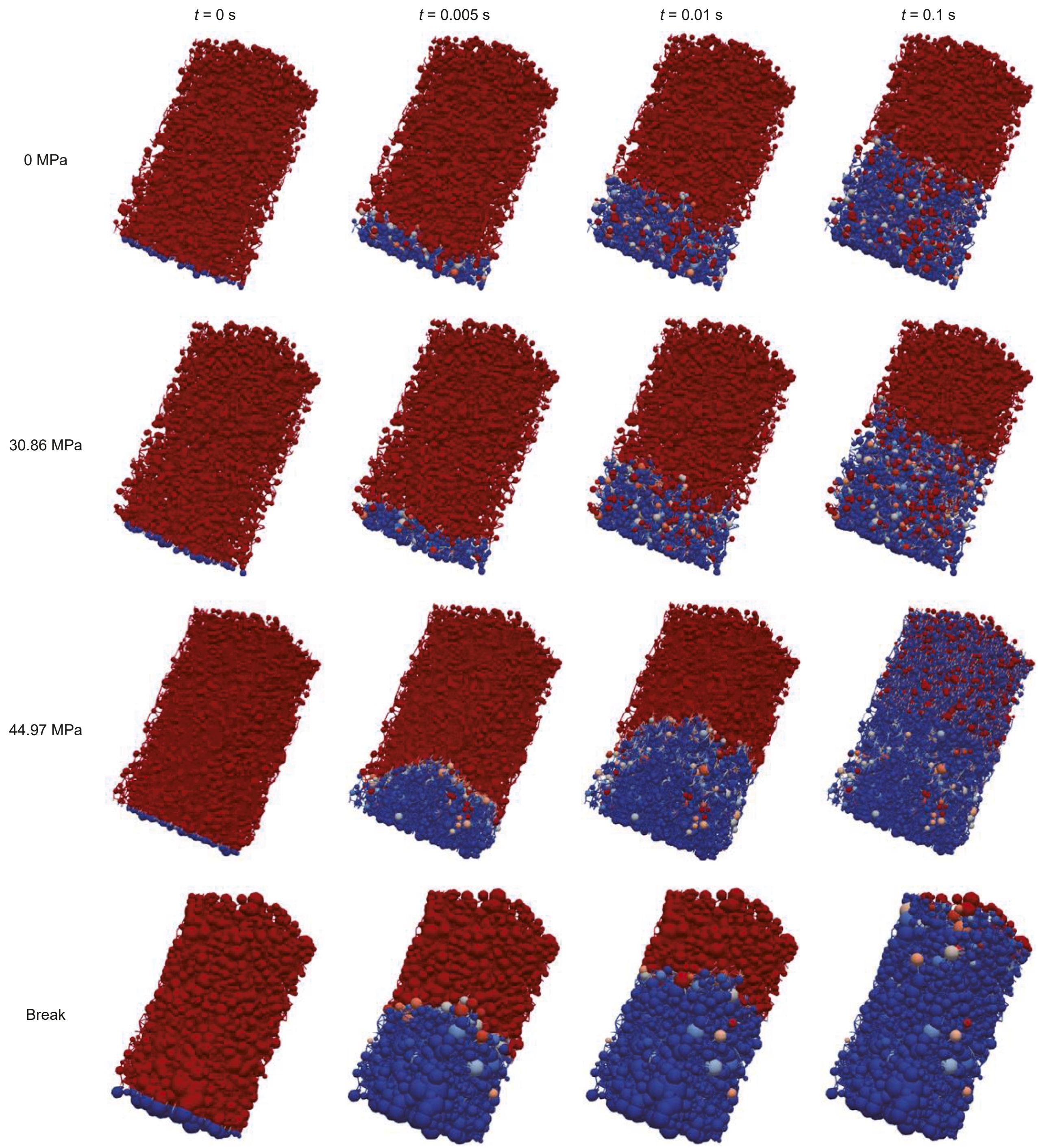

Fig. 5. Microscopic gas-water distribution in sandstone core under different stress conditions.

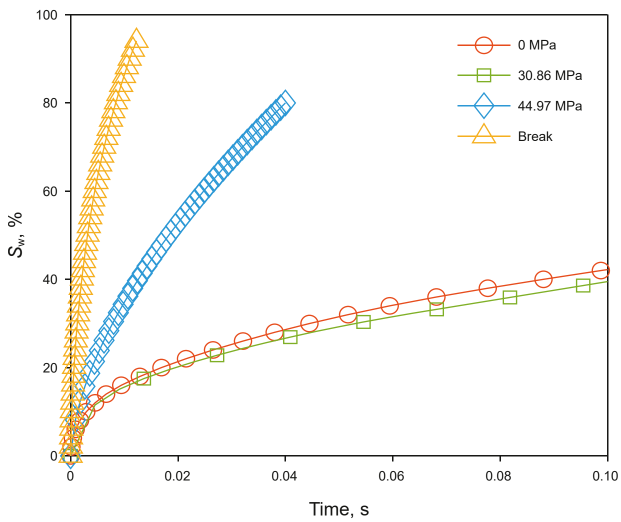

Fig. 6. Curves of water saturation with time under different stress conditions.

structure is more complex and interconnected, the water phase tends to migrate along pathways with lower resistance, resulting in a large amount of gas trapped in the large pores. When the stress increases to 44.97 MPa, the velocity of water invasion is accelerated and the displacement distance significantly extends. The formation of numerous connected throats at the lower section of the core enhances the efficiency of water invasion. After core failure, microfractures and pores are generated within the rock matrix, enlarging the gas–water contact area and providing additional flow pathways, which effectively facilitate the water invasion process. At the same time, the complexity of the pore space increases, and the gas clusters almost fill the entire pore space. Remaining gas is almost completely displaced from all types of pores, and the advancing water front exhibits a regular morphology.

The above analysis indicates that stress-induced pore structure evolution exerts a significant influence on the gas–water flow behavior in the core. During the elastic deformation stage, the variable diameter phenomenon in the core increases, leading to evident dynamic changes during the water invasion. At the front end of the core, a considerable amount of corner-type gas remains trapped in isolated pores with low coordination numbers. In the middle and rear sections, a large volume of gas is immobilized due to insufficient driving force, consequently forming dynamically trapped remaining gas. As the core enters the plastic deformation stage, the pores in the front section of the core gradually close, while a large number of throats emerge, and localized fracturing occurs at the rear end of the core. These structural changes intensify the heterogeneity of water invasion, causing a significant volume of gas to become trapped within larger pores in the downstream section of the core. Finally, in the fracture initiation and propagation stage, the spatial shape of the fracture is relatively simple. The water phase preferentially moves rapidly along the fracture surface, which accelerates the process of water invasion. The local pressure distribution between the fracture and the matrix is uneven, which induces the wetting water phase fluid to continuously imbibe from the fracture into the matrix, expanding the swept area of water invasion and mobilizing the trapped gas in the blind-end pores.

The variation curves of water saturation (S_w) in sandstone cores under different stress conditions are presented in Fig. 6. Prior to core failure, water saturation increases slowly with time at all stress levels. Under stresses of 0 MPa and 30.86 MPa, water saturation remains below 40% and 45% even after 0.1 s of displacement, indicating a relatively low water invasion rate. This behavior is attributed to the small pore sizes of the sandstone, which restrict available flow pathways and result in high flow resistance, leading to sluggish water invasion dynamics. When the applied stress increases to 44.97 MPa, the water invasion process is significantly accelerated, and water saturation rises rapidly to approximately 80% within 0.04 s. This indicates that stress-induced damage substantially enhances pore–throat connectivity and facilitates water migration. After core failure, fracturing occurs at the bottom of the core, generating a large number of newly connected throats and dominant flow channels. As a result, water saturation increases sharply from less than 10% to nearly 95% within 0.02 s. Correspondingly, the water invasion rate increases significantly, indicating that fractures become the dominant pathways for water invasion after failure.

The variation curves of water invasion rate with water saturation in sandstone cores under different stress conditions are shown in Fig. 7(a). Prior to rock failure, the influence of stress on

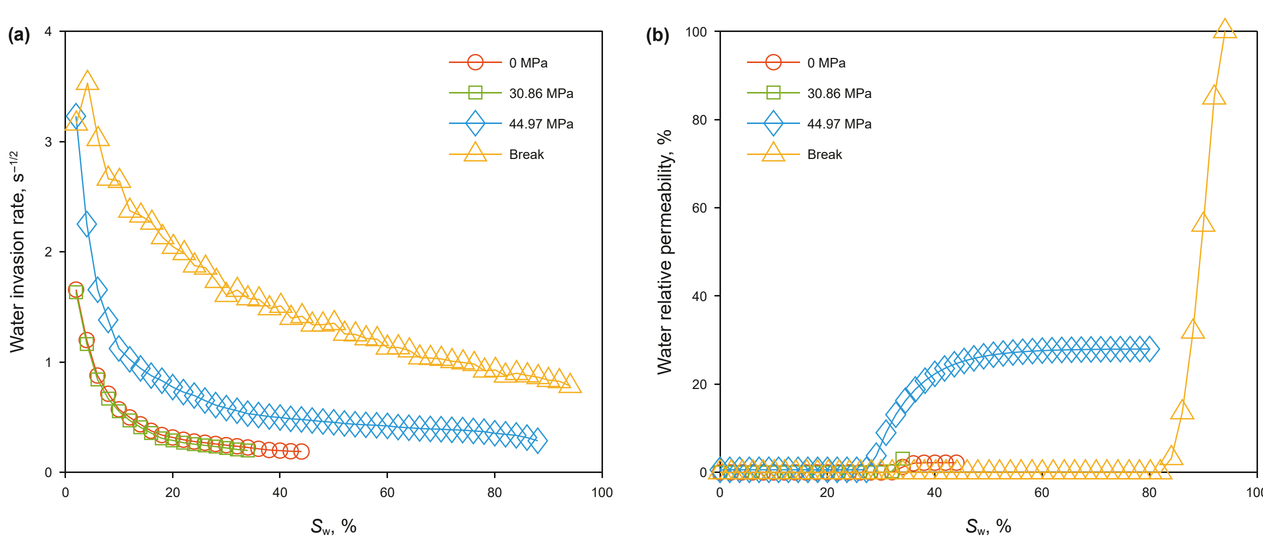

Fig. 7. Water-phase invasion rate and water relative permeability as functions of water saturation under different stress conditions. **(a)** Water invasion rate, **(b)** water relative permeability.

the water invasion rate is relatively minor. Under stresses of 0 MPa and 30.86 MPa, the water invasion rate decreases rapidly with increasing water saturation and falls below 0.1 $s^{-1/2}$ at $S_w > 30\%$, with little difference observed between the two stress levels, indicating that pore-scale flow resistance dominates the water invasion process before failure. When the applied stress increases to 44.97 MPa, the water invasion rate is markedly enhanced and remains at 0.5–0.7 $s^{-1/2}$. After core failure, the water invasion rate further increases, reaching a peak value of about 3.5 $s^{-1/2}$, indicating a significant acceleration of the overall water invasion process.

Fig. 7(b) shows the corresponding variation of water phase relative permeability with water saturation. Prior to core failure, the water phase relative permeability remains close to zero for all stress levels. At 44.97 MPa, it begins to increase at $S_w = 35\%$ and reaches a plateau value of 25%. After core failure, the water phase relative permeability increases sharply from less than 10% to nearly 100% as water saturation increases from 80% to 95%,

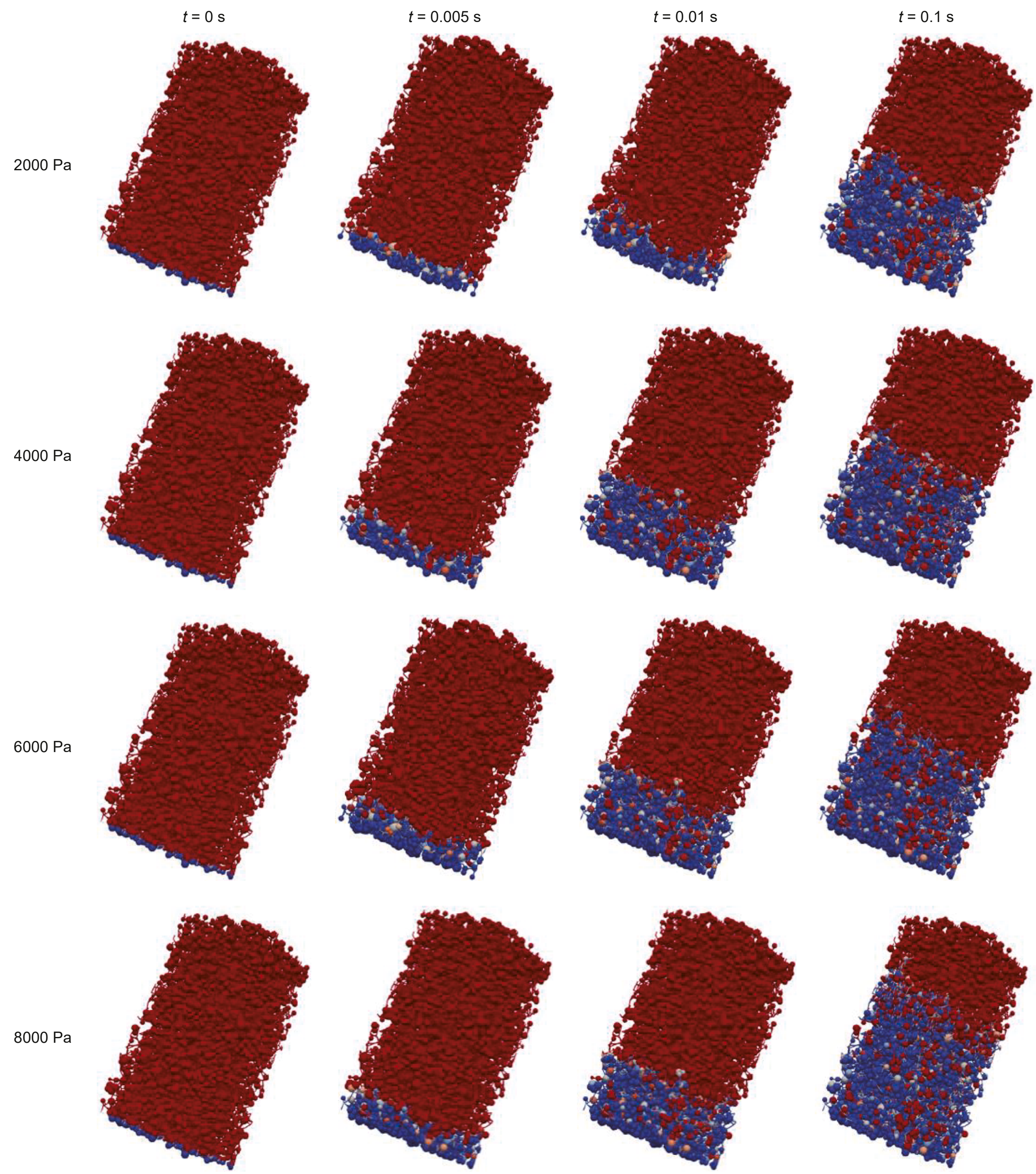

Fig. 8. Microscopic gas-water distribution in sandstone core under different displacement pressure differences.

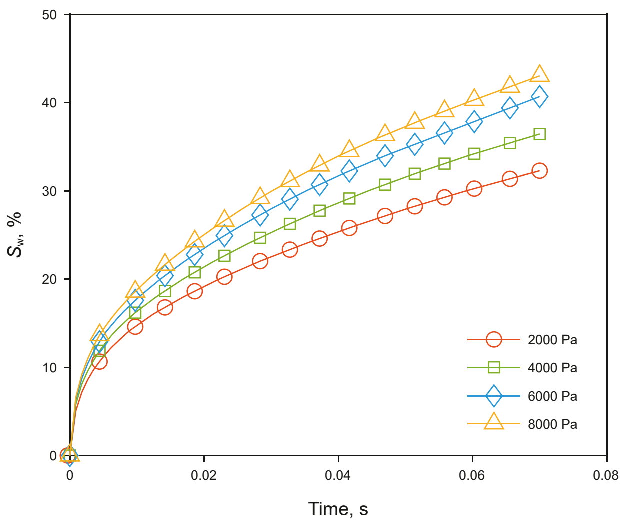

Fig. 9. Curves of water saturation with time under different displacement pressure differences.

reflecting a transition from pore-dominated flow to fracture-dominated flow.

4.2. Effect of displacement pressure difference

The water invasion behavior is significantly influenced by the displacement pressure difference. As the displacement pressure difference varies, different water invasion patterns are observed in the deep sandstone core. To further investigate this effect on gas-water distribution, dynamic pore network simulations are conducted on the core without applied stress loading, while keeping all other parameters constant. The displacement pressure differences are sequentially set to 2000, 4000, 6000, and 8000 Pa, and the results are shown in Fig. 8. Under all tested pressure conditions, the water front advances uniformly. When the displacement pressure difference is 2000 Pa, the water phase invades mainly along the primary flow channels, leaving remaining gas predominantly distributed within small, poorly connected pores. Due to the limited pressure propagation range, a portion of the gas remains trapped at the blind ends of pores, forming mainly corner-end and dynamically trapped remaining gas. When the displacement pressure difference increases to 4000 Pa, the migration speed of the displacement front accelerates. The types of remaining gas formed are basically the same as at 2000 Pa, mainly distributed in blind-end pores, poorly connected small pores, and the rear end of the core. When the displacement pressure difference increases to 6000 Pa, the speed of the water phase invading along the main channel further accelerates. Compared with smaller displacement pressure difference, the amount of gas trapped in the dead end of pores increases, and the water invasion front advances relatively uniformly. When the displacement pressure difference increases to 8000 Pa, the water invasion front advances more rapidly toward the central region of the core. However, under the influence of the high pressure difference, the formation water preferentially flows through the medium and large pores, resulting in these pores being gradually occupied by water. After the water establishes continuous flow channels, the invasion region ceases to expand and gradually reaches a steady state. This rapid channeling traps additional remaining gas, further intensifying the heterogeneity of water invasion.

The analysis indicates that as the displacement pressure difference increases, the migration velocity of the water front increases significantly, the displacement distance extends, and the non-uniformity of water invasion intensifies. The complex pore-throat connectivity governs the occurrence of remaining gas, which is predominantly composed of corner-end and dynamically trapped forms. Increasing the displacement pressure difference is ineffective in mobilizing these specific types of trapped gas.

Fig. 9 presents the variations in water saturation with time under different displacement pressure differences. During the early stage of water invasion ($t < 0.01$ s), the effect of displacement pressure difference on water saturation is limited, and the differences in water saturation among different pressure conditions are generally less than 3%. In this stage, water saturation rapidly increases to approximately 10%–15% for all cases. In the later stage of water invasion, water saturation exhibits a pronounced dependence on displacement pressure difference. At $t = 0.07$ s, the water saturation reaches approximately 32%, 36%, 39%, and 42% under displacement pressure differences of 2000, 4000, 6000, and 8000 Pa, respectively. Compared with the case of 2000 Pa, the final

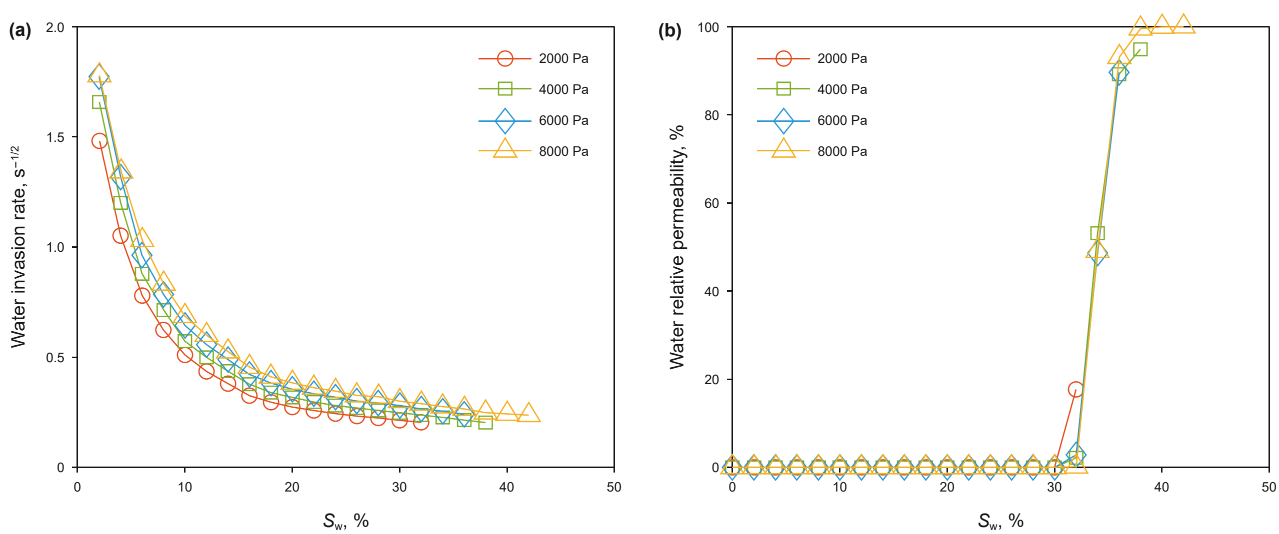

Fig. 10. Water-phase invasion rate and water relative permeability as functions of water saturation under different displacement pressure differences. **(a)** Water invasion rate, **(b)** water relative permeability.

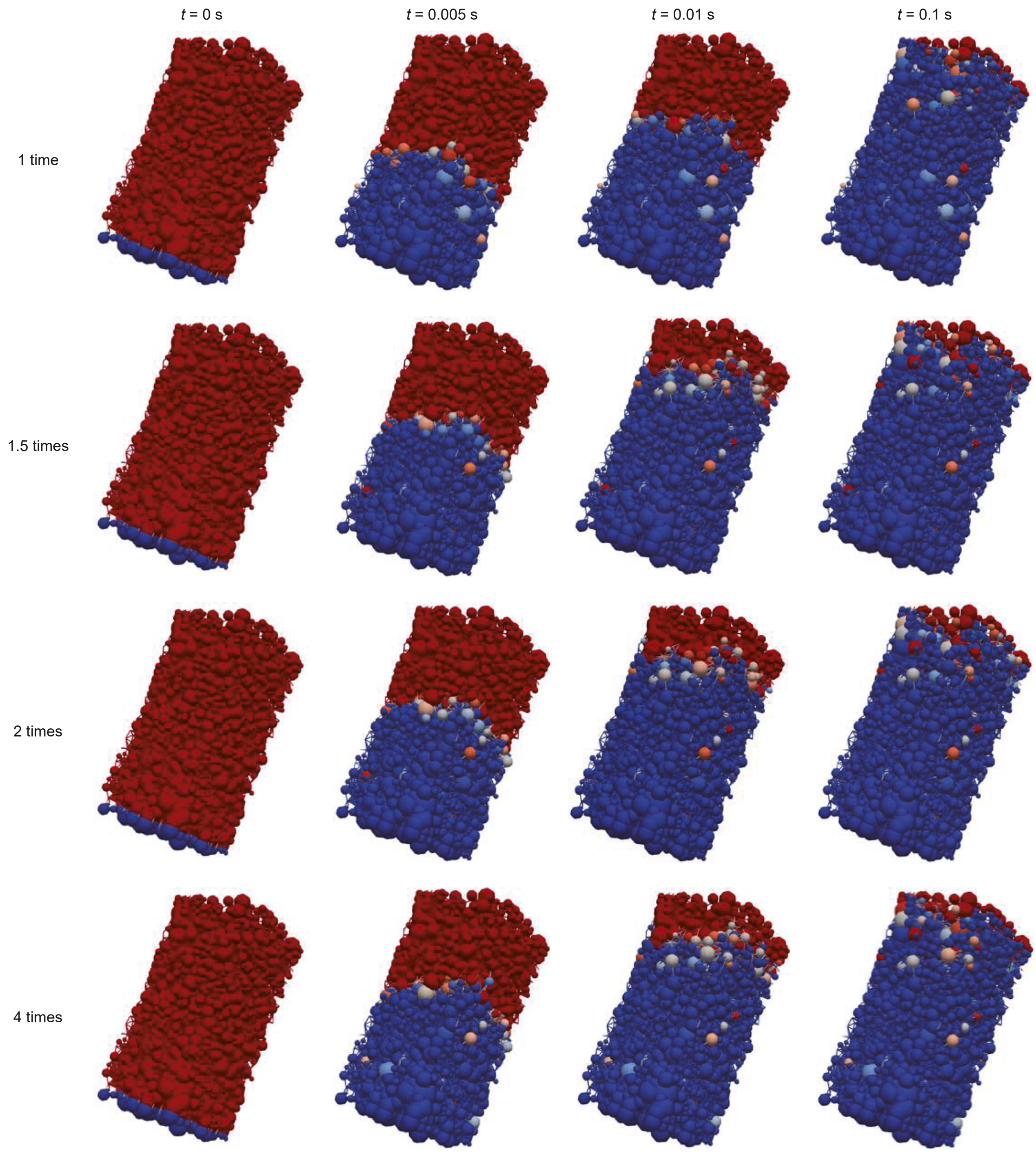

Fig. 11. Microscopic gas-water distribution in sandstone core under different fracture conductivities.

water saturation at 8000 Pa increases by about 10%. This behavior indicates that, during the early stage of water invasion, the invasion efficiency is mainly constrained by resistances induced by capillary forces and the Jamin effect. As the invasion progresses, these resistances gradually reach a dynamic balance, and the influence of displacement pressure difference on invasion efficiency becomes more pronounced, resulting in a significantly higher water saturation at larger pressure differences.

Fig. 10(a) shows the variation of water invasion rate with water saturation under different displacement pressure differences. In the early stage of water invasion (S_w < 10%), the water invasion rate decreases rapidly with increasing water saturation, and the differences among different displacement pressure differences remain relatively small. This suggests that the strong capillary effect associated with small pore radius initially masks the influence of displacement pressure difference on the water invasion rate. As water saturation increases (S_w > 20%), the water invasion rate gradually stabilizes, and the effect of displacement pressure difference becomes more evident. At S_w= 40%, the invasion rate under 8000 Pa remains 0.26 $s^{-1/2}$, indicating that a higher displacement pressure difference can partially maintain a higher invasion rate in the later stage.

Fig. 10(b) illustrates the corresponding variation of water-phase relative permeability with water saturation. During the initial stage of water invasion (S_w < 30%), the relative permeability of the water phase remains close to zero for all displacement pressure differences. When water saturation increases to 30%, the water-phase relative permeability increases sharply. At a water saturation close to 35%, the water-phase relative permeability under 8000 Pa reaches nearly 100%, whereas it is only about 20% under 2000 Pa, demonstrating a strong dependence on displacement pressure difference in the late stage of water invasion.

These results indicate that a higher displacement pressure difference enables the water phase to access more conductive flow paths, thereby enhancing the migration velocity of the invasion front and the relative permeability of the water phase. However, due to the small pore size and complex pore–throat structure of deep sandstone, local gas entrapment and the Jamin effect become increasingly significant, which limits the overall effectiveness of further increasing the displacement pressure difference.

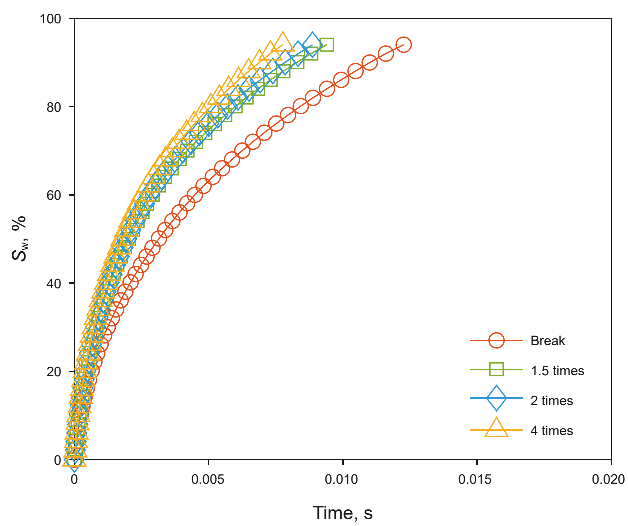

Fig. 12. Curves of water saturation with time under different fracture conductivities.

4.3. Effect of fracture conductivity

The fracture conductivity directly reflects the difficulty of fluid flow within fracture and is a key factor controlling production performance. To further investigate the effect of fracture conductivity on gas-water distribution, dynamic pore network simulations are carried out by sequentially changing the fracture conductivity to 1.5, 2, and 4 times the baseline value, while keeping all other parameters constant. The microscopic gas-water distribution in the sandstone core under different fracture conductivities is shown in Fig. 11.

At the baseline fracture conductivity, water invasion is primarily confined to the fracture-controlled region near the inlet, the invasion front remains relatively continuous. During the early stage of displacement, its propagation rate is limited, and lateral spreading into the surrounding pore network is weak. Gas accumulates above the advancing front, forming a continuous gas-rich region, and water invasion efficiency is constrained by limited fracture–matrix interaction. When the fracture conductivity increases to 1.5 times the baseline value, the water invasion front propagates more rapidly into the core and becomes thicker. Enhanced fracture conductivity improves hydraulic communication between fractures and the adjacent pores, promoting the simultaneous occurrence of fracture-dominated flow and matrix imbibition. Consequently, the invasion front exhibits a more regular morphology, while gas is progressively displaced and mainly trapped in blind-end pores and poorly connected pore spaces. With a further increase in fracture conductivity to 2 times the baseline value, the water invasion rate continues to increase, and the invasion front extends both axially and laterally. The strengthened fracture–matrix coupling enables more effective water penetration into the pore network. At this stage, the invasion front appears macroscopically stable, although pore-scale heterogeneity persists due to variations in local pore–throat connectivity. At the highest fracture conductivity (4 times the baseline value), water propagates rapidly along highly conductive fracture pathways, forming dominant axial flow channels. The temporal evolution of the gas–water distribution indicates that fracture-dominated channeling leads to fast upward propagation of the water phase, whereas matrix imbibition proceeds more slowly and lags behind fracture flow. At the late stage, the water phase

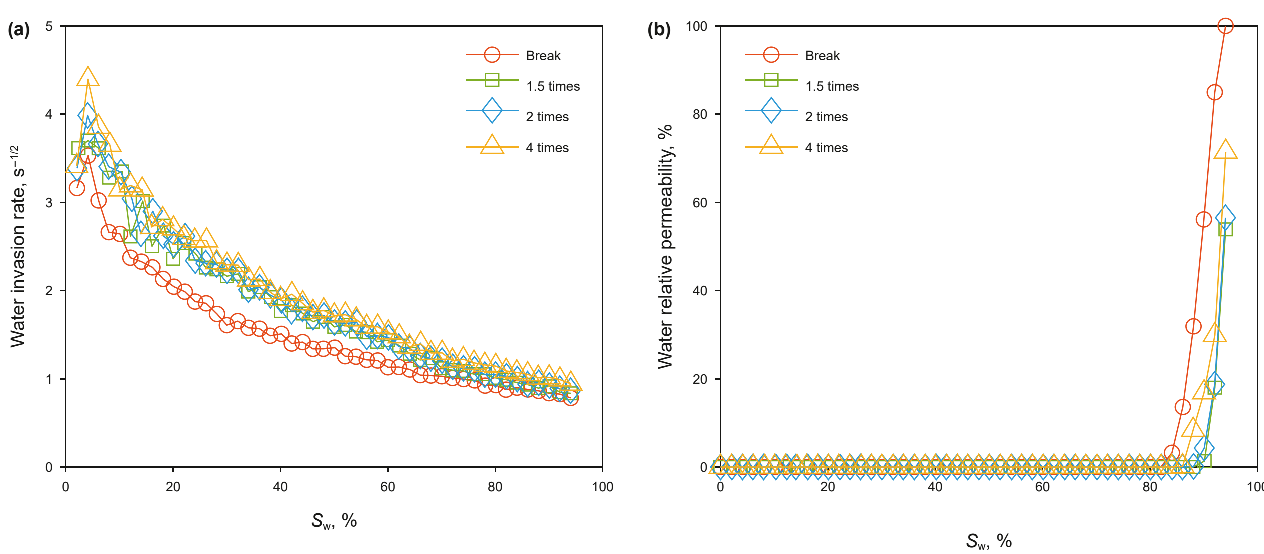

Fig. 13. Water-phase invasion rate and water relative permeability as functions of water saturation under different fracture conductivities. **(a)** Water invasion rate, **(b)** water relative permeability.

occupies most of the pore space, and the gas phase is largely displaced, leaving only a small number of isolated trapped clusters.

Overall, water invasion within the fracture–pore network exhibits a non-uniform advancement pattern during displacement, characterized by rapid fracture channeling accompanied by delayed matrix imbibition. Fracture conductivity governs the balance between these two processes, thereby exerting a dominant control on both the propagation rate and the morphological evolution of the water invasion front. Notably, comparison of the final gas–water distributions indicate that increasing fracture conductivity does not alter the fundamental types of remaining gas, which mainly consist of isolated trapped gas in blind-end pores and minor remaining gas near the downstream end of the core.

Fig. 12 presents the variations in water saturation over time under different fracture conductivity conditions. As the fracture conductivity increases, the water invasion rate accelerates. In contrast, fracture conductivity has little influence on the final water saturation, which remains within a narrow range of 94%–96% under all fracture conductivity conditions. These results indicate that fracture conductivity primarily affects the invasion rate rather than the ultimate water saturation of water invasion.

Fig. 13(a) shows the variation of water invasion rate with water saturation under different fracture conductivity conditions. At low water saturation (S_w < 20%), the invasion rate decreases rapidly with increasing saturation for all cases, and the differences among different fracture conductivities are relatively small. As water saturation increases, the effect of fracture conductivity becomes increasingly evident. At a water saturation of 50%, the invasion rate under the highest fracture conductivity (4 times) remains at 1.6 $s^{-1/2}$, compared with 1.3 $s^{-1/2}$ under the lowest conductivity (1 time), indicating that higher fracture conductivity sustains a higher invasion rate during the intermediate and late stages of invasion.

Fig. 13(b) presents the corresponding variation of water-phase relative permeability with water saturation. For all fracture conductivity conditions, the water-phase relative permeability remains close to zero at low water saturation and increases sharply when S_w exceeds 80%. As fracture conductivity increases, the rapid increase in water-phase relative permeability occurs at lower water saturation and proceeds more quickly. However, the final water-phase relative permeability remains similar for all cases, indicating that fracture conductivity mainly affects the transport rate rather than the ultimate extent of water invasion.

5. Conclusions

The ultra-deep sandstone core from the Tarim Basin is experimentally investigated using an in-situ stress loading CT system. Based on the experimental results, dynamic pore network simulations are conducted to analyze the influence of stress, pressure difference, and fracture conductivity on gas-water migration and distribution. The main conclusions are as follows:

(1) Stress-induced pore structure evolution is the primary control on gas–water migration, exceeding the influence of displacement pressure difference and fracture conductivity. In the absence of applied stress, water invades well-connected pores with a relatively uniform front, while gas remains trapped in poorly connected pores. Under low stress conditions (0–30.86 MPa), water saturation remains below 45% after 0.1 s of water invasion, and the water-phase relative permeability remains close to zero. As stress increases to 44.97 MPa, stress-induced damage significantly enhances pore–throat connectivity, accelerating water invasion and increasing water saturation to about 80% within 0.04 s. During plastic deformation and fracture initiation, the invasion pattern transitions from uniform to non-uniform. Once fractures initiate and propagate, water rapidly advances along fracture surfaces, and water saturation increases from less than 10% to 90% within 0.02 s.

(2) Increasing displacement pressure difference accelerates water invasion and propagation distance, with final water saturation increasing from 32% to 40% as pressure difference rises from 2000 Pa to 8000 Pa. However, due to complex pore–throat connectivity, strong capillary forces, and the Jamin effect, increasing the pressure difference alone is insufficient to effectively mobilize corner-bound and dynamically trapped gas. At high pressure differences, water preferentially flows through medium and large pores, forming dominant channels that enclose remaining gas and promote invasion non-uniformity.

(3) Fracture conductivity mainly controls the migration velocity and front morphology, while its effect on ultimate water saturation is limited. Increasing fracture conductivity up to four times the baseline raises the invasion rate to 1.6 $s^{-1/2}$ at 50% water saturation, compared with 1.3 $s^{-1/2}$ under the lowest fracture conductivity. Nevertheless, the final water saturation remains within a narrow range of 94%–96% for all fracture conductivity conditions. Higher conductivity advances the increase in water-phase relative permeability, but final values converge.

(4) Overall, stress-induced pore–fracture evolution governs non-uniform water invasion, preferential flow path development, early water breakthrough, and gas trapping in ultra-deep sandstone gas reservoirs. These findings provide mechanistic insight into stress-controlled water invasion and guidance for water control strategies. Nevertheless, the present study is limited by the laboratory-scale experimental setup and the spatial resolution of the CT imaging, and future work should extend to larger scales and integrate multi-scale observations.

CRediT authorship contribution statement

Fang-Zhou Liu: Writing – original draft, Visualization, Investigation. **Dai-Gang Wang:** Writing – review & editing, Formal analysis. **Yu-Shan Ma:** Resources, Investigation. **Ning-Hong Jia:** Resources, Methodology. **Jun-Lei Wang:** Methodology, Funding acquisition. **Chao-Zhong Qin:** Validation, Software, Methodology. **Fa Zhang:** Validation, Supervision. **Kao-Ping Song:** Project administration, Funding acquisition. **Yu-Hua Liu:** Visualization, Investigation. **Cheng-Ming Li:** Software, Resources.

Declaration of competing interest

No conflict of interest exists in the submission of this manuscript, and manuscript is approved by all authors for publication. I would like to declare on behalf of my co-authors that the work is original research unpublished previously, and not under consideration for publication elsewhere, in whole or in part. All the authors listed have approved the manuscript enclosed.

Acknowledgments

This research is financially supported by the National Natural Science Foundation of China (No. 52174043), the Beijing Natural Science Foundation (No. 3242019), the State Key Laboratory of Deep Oil and Gas (No. SKLD0G2024-KFZD-06), the CNPC

Innovation Foundation (No. 2022DQ02-0208), and the CNPC Major Scientific and Technological Program (No. 2023ZZ04).

References

Aker, E., Måløy, K.J., Hansen, A., 2000. Dynamics of stable viscous displacement in porous media. Phys. Rev. E 61 (3), 2936–2949. https://doi.org/10.1103/PhysRevE.61.2936.

Al-Zaidi, E., Edlmann, K., Fan, X., 2019. Gaseous CO_2 behaviour during water displacement in a sandstone core sample. Int. J. Greenh. Gas Control 80, 32–42. https://doi.org/10.1016/j.ijggc.2018.11.015.

An, S., Yao, J., Yang, Y., et al., 2016. Influence of pore structure parameters on flow characteristics based on a digital rock and the pore network model. J. Nat. Gas Sci. Eng. 31, 156–163. https://doi.org/10.1016/j.jngse.2016.03.009.

Ayachit, U., Bauer, A., Geveci, B., et al., 2015. Paraview catalyst: Enabling in situ data analysis and visualization. In: Proceedings of the First Workshop on in Situ Infrastructures for Enabling Extreme-Scale Analysis and Visualization, pp. 25–29. https://doi.org/10.1145/2828612.2828624.

Birdwell, J.E., Washburn, K.E., 2015. Multivariate analysis relating oil shale geochemical properties to NMR relaxometry. Energy Fuel. 29, 2234–2243. https://doi.org/10.1021/ef502828k.

Blunt, M.J., Bijeljic, B., Dong, H., et al., 2013. Pore-scale imaging and modelling. Adv. Water Resour. 51, 197–216. https://doi.org/10.1016/j.advwatres.2012.03.003.

Chen, R., Zhao, G., Xu, Y., et al., 2024. Coupled hydraulic–mechanical experimental system for evaluating dynamic mechanical and transport behaviors of deep rocks. Exp. Mech. 64 (6), 895–911. https://doi.org/10.1007/s11340-024-01063-z.

Collins, T.J., 2007. ImageJ for microscopy. Biotechniques 43 (S1), S25–S30. https://doi.org/10.2144/000112517.

David, C., Darot, M., Jeannette, D., 1993. Pore structures and transport properties of sandstone. Transport Porous Media 11, 161–177. https://doi.org/10.1007/BF01059632.

Duan, Y., Li, X., He, J., et al., 2018. Quantitative analysis of meso-damage evolution for shale under in situ uniaxial compression conditions. Environ. Earth Sci. 77, 1–9. https://doi.org/10.1007/s12665-018-7336-3.

Fang, F., Shen, W., Li, X., et al., 2019. Experimental study on water invasion mechanisms of fractured carbonate gas reservoirs in the Longwangmiao Formation, Moxi block, Sichuan Basin. Environ. Earth Sci. 78 (10), 316. https://doi.org/10.1007/s12665-019-8325-x.

Gostick, J., Khan, Z., Tranter, T., et al., 2019. PoreSpy: a python toolkit for quantitative analysis of porous media images. J. Open Source Softw. 4 (37), 1296. https://doi.org/10.21105/joss.01296.

Guo, C., Li, H., Tao, Y., et al., 2020. Water invasion and remaining gas distribution in carbonate gas reservoirs using core displacement and NMR. J. Cent. South Univ. 27 (2), 531–541. https://doi.org/10.1007/s11771-020-4314-1.

Han, D., Xiong, W., Jiang, T., et al., 2023. Investigation of the water-invasion gas efficiency in the Kela-2 gas field using multiple experiments. Energies 16 (20), 7216. https://doi.org/10.3390/en16207216.

Hu, A.P., She, M., Shen, A.J., et al., 2025. Visualization simulation experiments and porosity evolution mechanisms of deep to ultra-deep carbonate reservoirs. Petrol. Explor. Dev. 52 (2), 377–390. https://doi.org/10.1016/S1876-3804(25)60573-8.

Hu, J., Yang, S., Wang, B., et al., 2024. Effect of pore structure characteristics on gas–water seepage behaviour in deep carbonate gas reservoirs. Geoenergy Sci. Eng. 238, 212881. https://doi.org/10.1016/j.geoen.2024.212881.

Jia, A.L., Yan, H.J., Tang, H.F., et al., 2024. Key technologies and countermeasures for deep and ultra-deep gas reservoir development in China. Nat. Gas. Ind. 44 (1), 119–127. https://doi.org/10.3787/j.issn.1000-0976.2024.01.011 (in Chinese).

Joekar-Niasar, V., Prodanović, M., Wildenschild, D., et al., 2010. Network model investigation of interfacial area, capillary pressure and saturation relationships in granular porous media. Water Resour. Res. 46 (6), W06526. https://doi.org/10.1029/2009WR008585.

Li, G., Ren, W., Meng, Y., et al., 2014. Micro-flow kinetics research on water invasion in tight sandstone reservoirs. J. Nat. Gas Sci. Eng. 20, 184–191. https://doi.org/10.1016/j.jngse.2014.06.024.

Liu, F., Wang, D., Li, Y., et al., 2025. Pore-scale modeling of wettability alteration coupled two-phase flow in carbonate porous media. Chem. Eng. Sci. 302, 120854. https://doi.org/10.1016/j.ces.2024.120854.

Liu, G., Xie, S., Tian, W., et al., 2022. Effect of pore-throat structure on gas–water seepage behaviour in a tight sandstone gas reservoir. Fuel 310, 121901. https://doi.org/10.1016/j.fuel.2021.121901.

Liu, Q.M., Tang, H.F., Lu, Z.K., et al., 2023. Gas–water distribution and water invasion behavior under different fracture development models in ultra-deep gas reservoirs. Nat. Gas Geosci. 34 (6), 963–972. https://doi.org/10.11764/j.issn.1672-1926.2023.01.004 (in Chinese).

Lu, J.L., Lu, X.G., Wang, W., et al., 2019. Visualization experiment on gas–water distribution in tight sandstone. Special Oil Gas Reservoirs 26 (4), 136–141. https://doi.org/10.3969/j.issn.1006-6535.2019.04.024 (in Chinese).

Mason, G., Morrow, N.R., 1991. Capillary behavior of a perfectly wetting liquid in irregular triangular tubes. J. Colloid Interface Sci. 141 (1), 262–274. https://doi.org/10.1016/0021-9797(91)90321-X.

Qin, C.Z., Van Brummelen, H., 2019. A dynamic pore-network model for spontaneous imbibition in porous media. Adv. Water Resour. 133, 103420. https://doi.org/10.1016/j.advwatres.2019.103420.

Qin, C.Z., Van Brummelen, H., Hefny, M., et al., 2021. Image-based modeling of spontaneous imbibition in porous media by a dynamic pore network model. Adv. Water Resour. 152, 103932. https://doi.org/10.1016/j.advwatres.2021.103932.

Qin, C.Z., Wang, X., Zhang, H., et al., 2022. Numerical studies of spontaneous imbibition in porous media: Model development and pore-scale perspectives. J. Petrol. Sci. Eng. 218, 110961. https://doi.org/10.1016/j.petrol.2022.110961.

Shi, H., Zhu, Q., Chen, Z., et al., 2023. Pore-scale modeling of water–gas flow in heterogeneous porous media. Phys. Fluids 35 (7), 073301. https://doi.org/10.1063/5.0157655.

Shi, Y.P., Liu, Z.G., Wang, S.C., et al., 2024. Genetic mechanism and main controlling factors of high-quality clastic rock reservoirs in deep and ultra-deep layers. Petrol. Explor. Dev. 51 (3), 478–489. https://doi.org/10.1016/S1876-3804(24)60487-8.

Tang, L., Zhang, Y., Chen, X., et al., 2025. Multiscale gas flow mechanisms in ultra-deep fractured tight sandstone reservoirs with water invasion. Processes 13 (11), 3596. https://doi.org/10.3390/pr13113596.

Thompson, K.E., 2002. Pore-scale modeling of fluid transport in disordered fibrous materials. AIChE J. 48 (7), 1369–1389. https://doi.org/10.1002/aic.690480703.

Wang, J., Huang, Y., Zhou, F., et al., 2020. Reservoir damage during acidizing for high-temperature and ultra-deep tight sandstone. J. Petrol. Sci. Eng. 191, 107231. https://doi.org/10.1016/j.petrol.2020.107231.

Xiao, Q., Fang, F., Wang, Z., et al., 2019. Nuclear magnetic resonance simulation experiment for a water-drive gas reservoir. J. Energy Resour. Technol. 141 (11), 112901. https://doi.org/10.1115/1.4043636.

Xin, Y., Wang, G., Liu, B., et al., 2022. Pore structure evaluation in ultra-deep tight sandstones using NMR measurements and fractal analysis. J. Petrol. Sci. Eng. 211, 110180. https://doi.org/10.1016/j.petrol.2022.110180.

Xu, L., Zhang, W., Liang, X., et al., 2018. Grey correlation degree analysis of pore structure parameters of geotechnical media. J. Nanjing For. Univ. (Nat. Sci. Ed.) 54 (6), 1105–1113. https://doi.org/10.13232/j.cnki.jnju.2018.06.006 (in Chinese).

Yang, Y., Xu, Q., Li, X., et al., 2022. Pore-scale simulation of gas–water two-phase flow in volcanic gas reservoirs based on the volume of fluid method. J. Nat. Gas Sci. Eng. 106, 104733. https://doi.org/10.1016/j.jngse.2022.104733.

Zhang, L., Kang, Q.J., Yao, J., et al., 2015. Pore-scale simulation of liquid and gas two-phase flow based on digital core technology. Sci. China Technol. Sci. 58, 1375–1384. https://doi.org/10.1007/s11431-015-5842-z.

Zhang, T., Javadpour, F., Li, J., et al., 2021. Pore-scale perspective of gas/water two-phase flow in shale. SPE J. 26 (2), 828–846. https://doi.org/10.2118/205019-PA.

Zhang, T., Sun, T.L., Chen, W.H., et al., 2023. Pore-scale simulation of gas–water two-phase flow in carbonate reservoirs with different combinations of pore, network and vug. J. Southwest Petrol. Univ. (Sci. Technol. Ed.) 45 (5), 88–96. https://doi.org/10.11885/j.issn.1674-5086.2021.11.26.03 (in Chinese).

Zhang, Y., Yang, S., Zhang, Z., et al., 2022. Multiscale pore structure characterization of an ultra-deep carbonate gas reservoir. J. Petrol. Sci. Eng. 208, 109751. https://doi.org/10.1016/j.petrol.2021.109751.